Electronic conductance of a two-dimensional electron gas in the presence of periodic potentials

Y. Takagaki and D. K. Ferry
Center for Solid State Electronics Research, Arizona State University, Tempe, Arizona 85287-6202
(Received 13 November 1991)

We utilize mode-matching and transfer-matrix methods to study the transport properties of an electron through two-dimensionally modulated periodic potentials. The model structures treated here are finite-size one- and two-dimensional arrays of quantum boxes (lateral surface superlattice) and antidots. The structure is divided into a chain of uniform waveguide sections in the direction of current flow, and mode matching is imposed across the boundaries. The transfer-matrix technique is utilized to obtain the transmission probability for the composite superlattice structures. Energy dependences of the two-terminal conductance are presented in terms of the transition from one-dimensional to two-dimensional transport. Increasing the number of quantum boxes in the lateral surface superlattice shows that Lorentzian-shaped transmission resonances in a single quantum box are brought together to form a Bloch band structure. Complete reflections over broad energy ranges, due to the formation of minigaps, and a strong resonant behavior due to discrete states in minibands are observed in the energy dependence of the conductance. For the antidot lattice, the formation of the Bloch band structure is found to arise as a drop in the conductance. If attractive scattering centers are embedded in a two-dimensional electron gas, transmission resonances due to quasibound states are observed.

I. INTRODUCTION

There have been a considerable number of experimental and theoretical investigations on a periodically modulated two-dimensional electron gas (2DEG) in recent years.[1-5] The potential modulation introduces a Bloch band structure within the conduction band in the direction of the periodic potential. The Bloch electron is characterized by a characteristic length a, the periodicity of the potential being of the form $V(x)=V(x+a)$. An electron is Bragg reflected whenever integer multiples of the Fermi wavelength are equal to $2a$. Historically, Esaki and Tsu[6] proposed in 1970 a realization of energy gaps (minigaps) and bands (minibands) in a synthetic superlattice, which is created by an alternative growth of different semiconductors with different band-gap energies. Instead of the conventional superlattice, in which the periodic potential is produced perpendicular to a substrate, it is possible to achieve a lateral surface superlattice (LSSL) by use of multiple narrow gates in a field-effect transistor,[1] in which the potential modulation is defined in the plane of the 2DEG. The advantage is that the potential can be controlled by changing the bias applied to the gates. Owing to advances in microfabrication technology, it is now possible to create in-plane potential modulations of periodicity much smaller than the electron mean free path and the inelastic-scattering length. A manifestation of ballistic transport and phase coherence in split-gate devices has been demonstrated in recent experiments.[7]

In experiments on a one-dimensional (1D) LSSL, a grating gate is typically created on top of the heterostructure and the conductance is measured as a function of the gate voltage of the electrode, which tunes electron density and the amplitude of the potential modulation. A regular reproducible structure in the conductance has been revealed at low temperatures[2] and has been attributed to the Bragg reflection. However, because of the free-electron motion in the direction parallel to the 1D LSSL, all the occupied bands overlap at the Fermi energy. True gaps with zero density of states, which provide the clearest resonant structures in the conductance, are formed by creating two periodic potentials in a right angle. Although there are some experimental works[4,8] aimed at this subject, the interpretation of the observations in the 2D LSSL is not unambiguous. The analysis is not easy since it is considerably difficult to distinguish between the effects due to the formation of true minigaps and the effects that arise from quantum interference within a single quantum box. One of the ways to overcome this difficulty is to investigate a LSSL with a small number of unit cells. The miniband for the finite superlattice with N unit cells consists of a group of N almost dispersionless states, which merge into a continuous band in the limit $N\rightarrow\infty$.[9] The discretized minibands give rise to transmission resonances when energy is swept as a series of N peaks in the conductance. A theoretical analysis of the finite narrow 1D LSSL has been presented by Ulloa *et al.*[10] and the experimental observation has been reported by Kouwenhoven *et al.*[11]

In this paper, a complete description of an application of the waveguide-matching technique to the analysis of quantum-mechanical transmission through periodic potentials is given. We treat finite period 1D and 2D lateral superlattices and antidot lattices as model structures. We decompose the periodic potentials into successive waveguide sections in the longitudinal direction. The transmission probability through the entire system is evaluated numerically by use of a mode-matching method,[12] which characterizes the junctions, and the

transfer-matrix technique, which enables us to calculate the transmission through the cascaded waveguide. We have evaluated energy dependences of the conductance for the periodic potentials of various dimension. The formation of the Bloch band structure in the conduction band is shown by the appearance of regular structure in the conductance. Note that, although we restrict our discussion to the zero-magnetic-field regime, it is straightforward to include the presence of a perpendicular magnetic field in our numerical technique.

II. NUMERICAL APPROACH

In this section details of the numerical method are given for the 2D LSSL structure. A similar procedure is applied for the antidot structure, though some differences in the numerical procedure will be pointed out in Sec. III B. Typical model structures we discuss in this paper are sketched in Fig. 1. The global quantum waveguide consists of a finite strip defined by $(0<x<L,\ 0<y<W)$, in which periodic potential modulations are taken into account, and two semi-infinite strips defined by $(-\infty<x<0,\ 0<y<W)$ and $(L<x<\infty,\ 0<y<W)$, which are connected to two reservoirs at each end. We ignore inelastic scattering throughout the device. The Schrödinger equation for a noninteracting 2DEG in the effective-mass approximation is

$$\left[-\frac{\hbar^2}{2m}\left[\frac{\partial^2}{\partial x^2}+\frac{\partial^2}{\partial y^2}\right]+V_c(y)+V(x,y)\right]\Psi(x,y) = E\Psi(x,y)\ , \quad (1)$$

where m is the electron effective mass, $V_c(y)$ represents a confining potential in the direction perpendicular to the current flow, and $V(x,y)$ is the periodic potential. From now on, we assume that the potential modulation is characterized by a δ function, for simplicity. Therefore, we have

$$V(x,y)=U_x\sum_{j=0}^{N_x}\delta(x-ja)+U_y\sum_{j=0}^{N_y}\delta(y-ja) \quad (2a)$$

$$\equiv V_x(x)+V_y(y)\ , \quad (2b)$$

where a is the dimension of an individual quantum box. The device geometry is chosen such that we have $N_x a=L$ and $N_y a=W$. In experiments on the LSSL, the superlattice potential is typically produced by applying negative bias to the grating or grid gate, so that a modulation described by a sine function may be realistic because of the screening. We note that our method can easily be extended to treat a Kronig-Penney-type potential and the proper choice of the potential is not essential to the following discussion. The LSSL structure is separated for each period in the x direction into N_x uniform waveguide sections. The mode matching is considered across the junctions $x=ja$ $(j=0,1,\ldots,N_x)$, where the δ-function potential occurs. The generalized continuity condition for the wave function and its normal derivative gives a matrix which relates the amplitudes between modes in the left-hand side and right-hand side semi-infinite strips.

Consider transmission and reflection properties of an electron with energy E_F incident on the 2D LSSL potential. The wave vector has a longitudinal component along the x axis and a transverse component along the y axis, which is quantized in the finite width channel. The general solution of the wave function in each waveguide segment is given in terms of a superposition of the eigenmodes $\chi_n(y)$ in the y direction:

$$\Psi(x,y)=\sum_n \phi_n(x)\chi_n(y)\ , \quad (3)$$

where $\chi_n(y)$ satisfy a 1D Schrödinger equation:

$$\left[-\frac{\hbar^2}{2m}\frac{d^2}{dy^2}+V_c(y)+V_y(y)\right]\chi_n(y)=E_n\chi_n(y)\ , \quad (4)$$

where E_n are the subband energies. Throughout this paper, we assume hard-wall confinement along the guide edge walls. Therefore, in the two semi-infinite strips, or in the absence of the superlattice potential in the y direction ($U_y=0$), the eigenfunctions have the form

$$\chi_n(y)\equiv u_n(y)=\sqrt{2/W}\ \sin\left[\frac{n\pi}{W}y\right]\ . \quad (5)$$

The eigenfunctions in the uniform waveguide section

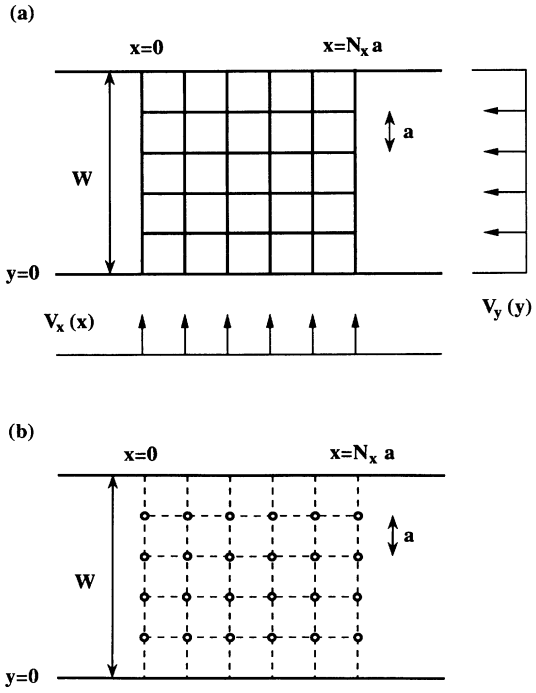

FIG. 1. Schematic view of the electron waveguides with presence of finite-size periodic potential modulations. (a) 2D lateral surface superlattice and (b) 2D array of antidots (indicated by open circles) with $N_x=N_y=5$. δ-function potentials are assumed in the calculation. The device is divided into N_x+2 uniform waveguide sections and the wave function is matched across the boundaries at $x=la$.

when $V_y(y)\neq 0$ are expanded in terms of $u_n(y)$:

$$\chi_n(y)=\sum_l f_{nl}u_l(y) \ . \tag{6}$$

The expansion coefficients f_{nl} are given by the following eigenvalue equation:

$$\sum_j (l^2\delta_{jl}+K_{jl})f_{nj}=\frac{2mW^2}{\pi^2\hbar^2}E_n f_{nl} \ , \tag{7}$$

where

$$K_{jl}=\frac{2mW^2}{\pi^2\hbar^2}\int u_j(y)V_y(y)u_l(y)dy \tag{8a}$$

$$=\begin{cases}\alpha N_y \ , & |l+m|=2iN_y \text{ and } l+m\neq 2jN_y \\ -\alpha N_y \ , & |l-m|\neq 2iN_y \text{ and } l+m=2jN_y \\ 0 \quad \text{otherwise} \ , \end{cases} \tag{8b}$$

with $\alpha=2mWU_y/\pi^2\hbar^2$ and $i,j=0,1,2,\ldots$. The eigenfunctions are supposed to be normalized and thus satisfy the orthogonality relation

$$\sum_l f_{il}f_{jl}=\delta_{ij} \ . \tag{9}$$

Figure 2 gives the lowest seven subband thresholds as a function of the dimensionless strength of the superlattice potential $U_s=mWU_y/\pi^2\hbar^2$ for the uniform waveguide section with $N_y=5$. With increasing U_s, eigenstates in the periodic potential come together into groups of N_y subbands, which are closely spaced in energy and eventually degenerate in the limit $U_s\rightarrow\infty$. The eigenenergies for the modes with integer index multiples of N_y are unaffected by the potential and thus correspond to those for $U_s\rightarrow\infty$.

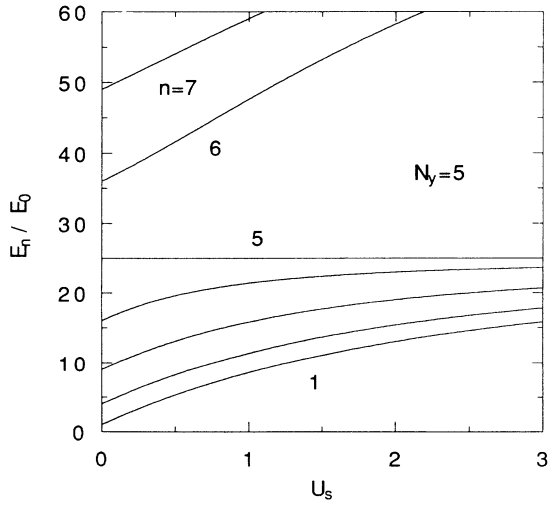

FIG. 2. The subband thresholds for the first seven modes as a function of the dimensionless strength of the superlattice potential U_s. The quantity E_0 is $\pi^2\hbar^2/2mW^2$, and so the values of E_n/E_0, are n^2 when $U_s=0$. The number of unit cells is $N_y=5$, so that the lower four subbands come closer to the $n=5$ subband as U_s is increased.

The normal derivative of the wave function across the boundary of the uniform waveguide sections is no longer continuous whenever $U_x\neq 0$. We need to derive generalized boundary conditions applicable when the δ-function potential is present. The wave function (3) can be expressed in terms of the eigenstates $u_n(y)$ of the perfect lead as

$$\Psi(x,y)=\sum_{n,l}\phi_n(x)f_{nl}u_l(y)\equiv\sum_l c_l(x)u_l(y) \ . \tag{10}$$

Substituting (10) into (1), and using the orthogonality property, we have

$$\frac{d^2c_l(x)}{dx^2}+k_l^2c_l(x)=\sum_m V_{ml}(x)c_m(x) \ , \tag{11}$$

where

$$k_l=\sqrt{k_F^2-(l\pi/W)^2} \tag{12}$$

and $V_{ml}(x)$ represent the coupling between mode m and l:

$$V_{ml}(x)=\frac{2m}{\hbar^2}\int u_m(y)V(x,y)u_l(y)dy \ . \tag{13}$$

Integrating (11) once gives a generalized boundary condition at $x=ja$ for the LSSL potential given by (2):[13]

$$\left.\frac{dc_l(x)}{dx}\right|_{x=ja+\varepsilon}-\left.\frac{dc_l(x)}{dx}\right|_{x=ja-\varepsilon}=\frac{2mU_x}{\hbar^2}c_l(ja) \ . \tag{14}$$

We also see that the continuity of the wave function itself is preserved.

In the regions $[(j-1)a<x<ja]$ and $[ja<x<(j+1)a]$, where $V(x,y)$ is independent of x, the solution to (1) is given as

$$\Psi(x,y)=\sum_{l,m}(A_l e^{iq_l[x-(j-1)a]}+B_l e^{-iq_l(x-ja)})g_{lm}u_m(y)$$

$$[(j-1)a<x<ja] \ , \tag{15a}$$

$$\Psi(x,y)=\sum_{l,m}(C_l e^{ip_l(x-ja)}+D_l e^{-p_l[x-(j+1)a]})h_{lm}u_m(y)$$

$$[ja<x<(j+1)a] \ , \tag{15b}$$

where wave vectors q_l and p_l are given by

$$q_l=\frac{\sqrt{2m(E_F-E_l)}}{\hbar} \ , \quad p_l=\frac{\sqrt{2m(E_F-E_l)}}{\hbar} \ , \tag{16}$$

with E_l the subband energies in corresponding uniform waveguide section. The values g_{lm} and h_{lm} are determined by (7). The sum over l and m is cut off at a practical limit in the numerical calculation and needs to include evanescent modes for which the wave vector is imaginary. Imposing the boundary conditions at $x=ja$, one obtains the relation

$$C_n=\tfrac{1}{2}\sum_{l,m} g_{lm}h_{nm}\left[\left[1+\frac{q_l-i\beta}{p_n}\right]e^{iq_l a}A_l+\left[1-\frac{q_l+i\beta}{p_n}\right]B_l\right], \tag{17a}$$

$$D_n=\tfrac{1}{2}\sum_{l,m} g_{lm}h_{nm}\left[\left[1-\frac{q_l-i\beta}{p_n}\right]e^{i(q_l-p_n)a}A_l+\left[1+\frac{q_l+i\beta}{p_n}\right]B_l e^{-ip_n a}\right], \tag{17b}$$

where $\beta=2mU_x/\hbar^2$. Repeating this mode-matching procedure, we can obtain the relation between modes in the entrance and the exit of the LSSL. If the wave function in the left-hand-side semi-infinite strip has the form

$$\varphi_n^{(\pm)}=e^{\pm ik_n x}, \tag{18}$$

i.e., only one of the incoming or outgoing modes in the perfect lead is occupied, the wave function in the right-hand-side semi-infinite strip may generally be described as

$$\varphi_n^{(\pm)}=\sum_m (I_{mn}^{(\pm)}e^{ik_m x}+J_{mn}^{(\pm)}e^{-ik_m x}). \tag{19}$$

The coefficients $I_{mn}^{(\pm)}$ and $J_{mn}^{(\pm)}$ are calculated using (17).

When an electron is incident through mode n, the wave function is given in terms of a superposition of one right-moving and all left-moving waves:

$$\varphi_n^{(\pm)}=e^{ik_n x}+\sum_m r_{mn}e^{-ik_m x}, \tag{20}$$

where r_{mn} is the reflection amplitude from mode n to mode m in the left-hand-side lead. Using (18)–(20), the wave function in the right-hand-side lead is given as

$$\varphi_n^{(\pm)}=\sum_m\left[I_{mn}^{(+)}+\sum_l r_{ln}I_{ml}^{(-)}\right]e^{ik_m x}+\sum_m\left[J_{mn}^{(+)}+\sum_l r_{ln}J_{ml}^{(-)}\right]e^{-ik_m x}. \tag{21}$$

This should contain only right-moving waves with amplitudes t_{mn}, which represent the transmission amplitude from mode n in the left-hand-side lead to mode m in the right-hand-side lead. Therefore, this mode-matching procedure results in the following equations:[14]

$$I_{mn}^{(+)}+\sum_l r_{ln}I_{ml}^{(-)}=t_{mn}, \tag{22a}$$

$$J_{mn}^{(+)}+\sum_l r_{ln}J_{ml}^{(-)}=0. \tag{22b}$$

By solving (22), one can evaluate the transmission and reflection coefficients T_{mn} and R_{mn} as

$$T_{mn}=\frac{k_m}{k_n}|t_{mn}|^2, \tag{23a}$$

$$R_{mn}=\frac{k_m}{k_n}|r_{mn}|^2. \tag{23b}$$

The two-terminal conductance of the system is given by the linear conductance formula[15]

$$G=\frac{2e^2}{h}\sum_{m,n}T_{mn}, \tag{24}$$

where the sum runs only over the propagating modes.

For the usual mode-matching technique, a system of linear equations for the expansion coefficients like those in (15) needs to be solved for each incident mode. This is unfavorable when there are many modes below the Fermi energy in the perfect lead. The number of equations, i.e., the size of the matrix, which characterizes the system, increases with an increasing number of uniform waveguide sections. For the technique utilized in this paper, however, the conductance is easily given once $I_{mn}^{(\pm)}$ and $J_{mn}^{(\pm)}$ are obtained, and the number depends only on the total number of modes taken into account, in other words, independent of the number of uniform waveguide sections. Therefore, the transfer-matrix technique remarkably saves CPU time.

III. RESULTS AND DISCUSSION

In this section we present numerical results for the conductance of lateral superlattices and arrays of antidots as shown in Fig. 1. The energy dependences of the two-terminal conductance are evaluated for various dimension lattices. In the following examples, the width of the external leads is assumed to be the same with that of the superlattice region. In reality, an appropriate choice of the junction geometry depends on the experimental setup. For the 2D LSSL, the artificially imposed hard-hall boundary condition should not affect the results. On the other hand, a coupling of the narrow channel to the external system with large width induces strong mode mixing.[16] The overall trend of the structures in the conductance is, however, supposed to be robust against the details of the injection process.[10]

A. Lateral surface superlattice

For the 1D LSSL ($N_y=1$ or $U_y=0$), we have $g_{lm}=h_{lm}=\delta_{lm}$ and $q_l=p_l=k_l$. Therefore, (17) is reduced to

$$C_n=\left[1-i\frac{\beta}{2k_n}\right]e^{ik_n a}A_n-i\frac{\beta}{2k_n}B_n, \tag{25a}$$

$$D_n=i\frac{\beta}{2k_n}A_n+\left[1+\frac{\beta}{2k_n}\right]e^{-ik_n a}B_n. \tag{25b}$$

An electron impinging on the superlattice potential is partially transmitted or reflected within the same mode, i.e., there is no mixing of electron states between the subbands for the 1D superlattice potential and each 1D subband carries current independently. The orthogonality relation (9) gives a similar result across the boundaries for the 2D LSSL except $x=0$ and $x=L$. Therefore, we can say that the superlattice potential in the x direction induces multiple reflections, while that in the y direction causes mode mixing at the entrance and the exit of the

LSSL structure. In the following, we assume an identical dimensionless barrier potential U_s in two orthogonal directions.

As a first example, we consider the simplest geometry, i.e., a single quantum box connected to two ideal leads on both sides. For large barrier potentials, the device becomes a zero-dimensional box with discrete levels in the three spatial directions. The quasibound states in the quantum box are expected to show strong transmission resonances when the Fermi energy aligns with the bound-state energy. The number of potential variations in the x direction is reduced to two in Fig. 3. We plot the conductance of coupled parallel quantum boxes ($N_x=1$) as a function of Fermi wave vector k_F and the periodicity of the lattice a. The dimensionless parameter $k_F a/\pi$ counts the number of subbands below the Fermi energy in a unit cell. If we take $a=100$ nm, the sheet electron concentration of 2DEG to fulfill $k_F a/\pi=1$ is $n_s=1.6\times10^{14}$ m^{-2}. When $N_y=1$, one can see distinct sharp resonances with an amplitude $2e^2/h$. This resonant conduction through the zero-dimensional states defined between barriers arises from a similar mechanism to tunneling phenomena found in resonant tunneling diodes. When N_y is increased, the resonance splits into N_y peaks corresponding to nearly degenerate states in the y direction. An oscillation in the conductance, which is interpreted in terms of resonant tunneling via localized states in the quantum box, has been observed experimentally in double barrier[17] and double constriction[18] geometries. Smith *et al.* have observed (in the double-barrier geometry) large oscillations due to resonant conduction through zero-dimensional states when the negative gate voltage is strong and a series of small peaks for weak negative gate voltage.[17]

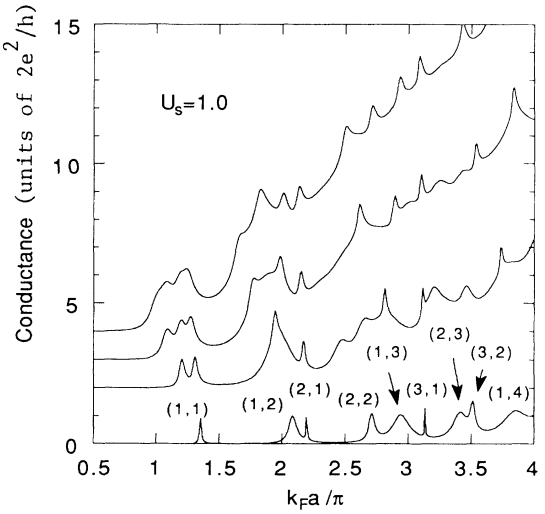

FIG. 3. Conductance (in units of $2e^2/h$) as a function of $k_F a/\pi$ for coupled parallel quantum boxes ($N_x=1$). Each curve corresponds, from top to bottom, to $N_y=4$ to $N_y=1$, respectively. The peak indexes (n,m) (see text) are indicated for the conductance of a single quantum box (lowest curve). The resonances split into multiple peaks when N_y is increased due to degeneracy in the y direction. The strength of the potential considered, which is assumed to be identical in two directions, is $U_s=1.0$. The higher three curves are offset by $4\times2e^2/h$, $3\times2e^2/h$, and $2\times2e^2/h$ for clarity.

Since there is no mode mixing when $N_y=1$, the conductance is given by the sum of contributions of individual channels. The transmission probability for the n mode is analytically obtained. If the asymmetry of the amplitude of the left and right barriers is taken into account as U_L and U_R, one obtains

$$|T(k_n)|^2=\frac{\Gamma_L\Gamma_R}{1+(1+\Gamma_L)(1+\Gamma_R)-2\sqrt{(1+\Gamma_L)(1+\Gamma_R)}\cos(2k_n a+\delta)}\ , \tag{26}$$

where $\Gamma_\mu=(\gamma_\mu)^2=(\hbar^2k_n/mU_\mu)^2$ are leak efficiency to the leads and $\tan(\delta)=(\gamma_L+\gamma_R)/(1-\gamma_L\gamma_R)$. It may be noteworthy that (26) is independent of the polarity of U except for the sign of δ. In the weak link limit ($\Gamma_L,\Gamma_R\to0$), (26) can be approximated by

$$|T|^2\sim\frac{\Gamma_L\Gamma_R}{\frac{1}{4}(\Gamma_L+\Gamma_R)^2+2[1-\cos(2k_n a)]}\ . \tag{27}$$

The energies at which the maximum of transmission occurs are given by

$$\frac{k_F W}{\pi}=\sqrt{m^2+n^2}\quad(m=1,2,\ldots)\ . \tag{28}$$

If the resonances are well separated in energy, a single quasibound state in the quantum box gives a resonance of the form of a Lorentzian centered around the resonance energy.[19] At resonances the transmission coefficient approaches unity when the barrier is symmetric, while it is reduced for an asymmetric barrier by up to a factor $4\Gamma_R/\Gamma_L$ if $\Gamma_L\gg\Gamma_R$. The larger the resonance indices m, the broader the peak width and the lower the resonant energy below the prediction of (28). The sets of indices (n,m) corresponding to peaks are denoted in Fig. 3 for the lowest curve. Even for the symmetric quantum box, splitting of levels due to leaks in the x direction are seen in Fig. 3. The details of the position of the peaks in energy are strongly sensitive to an asymmetry in the sample dimensions in the two orthogonal directions. In the limit $W\to\infty$, the conductance is given by taking a sum over n of (28). Because of a free-electron motion in the y direction, a single resonance has a shape of $G(E)\propto(E-E_r)^{-1/2}$, where E_r is the resonance energy, instead of the Lorentzian.

The lowest curve in Fig. 4 shows the conductance of narrow 1D LSSL as a function of energy for a sequence

of four coupled quantum boxes. Within the nearly-free-electron approximation, the width of the nth minigap is approximately $\Delta E_n \approx 2U_n$, with U_n the amplitude of the Fourier component of the potential at wave vector $k_n = 2\pi n/a$. For a sine potential, the minigap opens only for $n = 1$. On the other hand, the width of the minigap is independent of n for a δ-function potential. It is clear that the electron is Bragg reflected when the Fermi energy lies in the gaps between the discrete states in the miniband for the finite LSSL. The number of oscillations in the conductance separated by broad minima due to minigaps is equal to the number of quantum boxes N_x.[10] The minibands associated with $(n,m)=(1,2)$ and $(2,1)$ overlap at $k_F a/\pi \approx 2.2$ and therefore the width of the peak of the former is wider than that of the latter. The formation of minibands and minigaps in a finite LSSL has been reported using corrugated split-gate structures, in which the 1D LSSL is realized by a periodic modulation of the constriction width instead of the potential modulation.[11] A regular structure in the conductance associted with the formation of the discrete miniband has been observed. We note that the experiment was performed in the quantized Hall regime so that it is supposed that the coupling to the external 2DEG is almost adiabatic and mode mixing due to width variation is less important.

The conductance of the 2D LSSL is plotted in Fig. 4 for up to $N_y = 5$. When the potential modulation is weak, the conductance increases in steps of $2e^2/h$ due to contact resistance.[20] When the amplitude of the potential modulation is increased, one can see broad regions of zero conductance, corresponding to the formation of minigaps, and rapid oscillations due to minibands. In the 2D LSSL, N_y quantized plateaus, which split into N_x peaks, group into the miniband and the minigap develops before the next miniband. The energies at which minigaps open are nearly independent of N_y when the energy

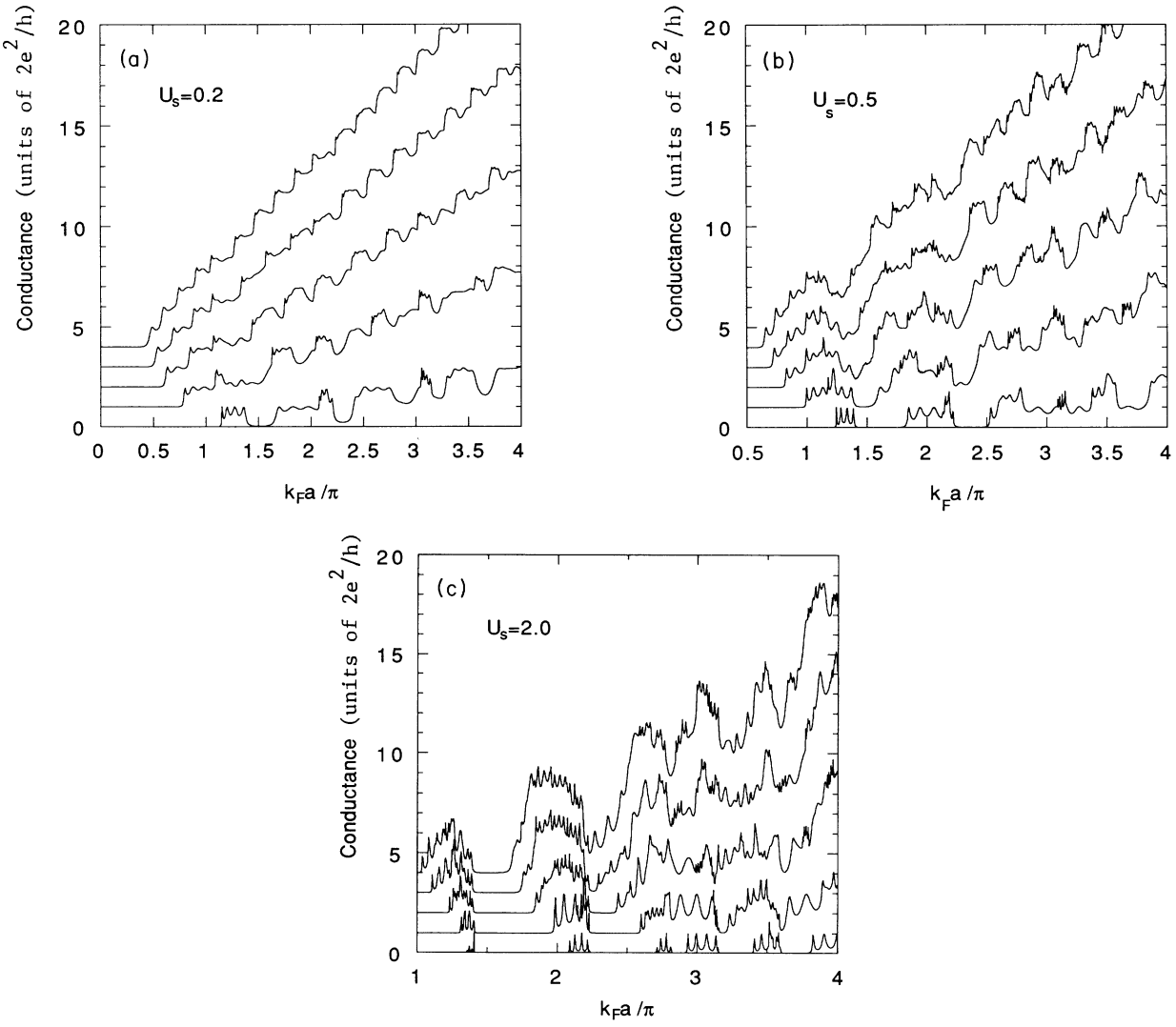

FIG. 4. Conductance (in units of $2e^2/h$) as a function of $k_F a/\pi$ for finite period superlattices with $N_x = 4$. Each curve, from top to bottom, corresponds to $N_y = 5$ to $N_y = 1$, respectively. The strength of the potential considered is (a) $U_s = 0.2$, (b) $U_s = 0.5$, and (c) $U_s = 2.0$. Broad dips due to the formation of minigaps and rapid oscillations due to the N_x discrete states in minibands are visible. The higher edge of the minibands is independent of U_s and N_y. The curves are offset by $2e^2/h$.

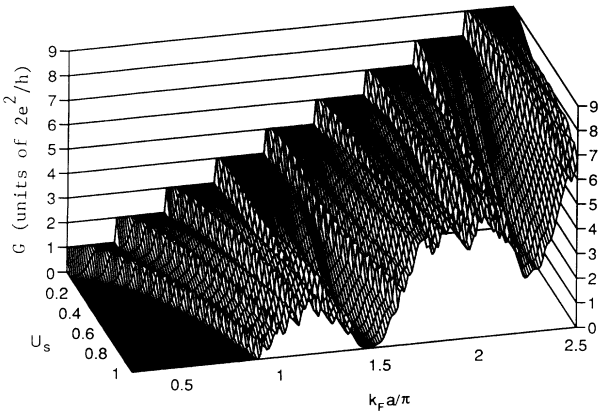

FIG. 5. Conductance (in units of $2e^2/h$) for a two-dimensional lateral surface superlattice with $N_x=N_y=4$ as functions of U_s and k_Fa/π. When the superlattice potential is introduced, N_y subbands merge into a miniband and minigaps open between the minibands. The lower edge of the minibands becomes higher in energy as U_s is increased.

is measured in terms of k_Fa/π. As shown in Fig. 5, the propagation threshold of each subband, thus the lower edge of the minibands, becomes higher in energy when U_s is increased, whereas the higher edge of the minibands, which is determined by (28), are effectively independent of U_s. A total reflection is clearly observed for energies near $k_Fa/\pi=1.5$ [corresponding to $(n,m)=(1,1)$] and 2.3 [corresponding to $(n,m)=(1,2)$ and $(2,1)$]. The quantum box in the 2D LSSL couples with other quantum boxes, giving rise to a quasibound state instead of a true bound state. The appearance of quasibound states gives rise to sharp resonances in transmission probability. When the barrier potential is increased, the quantum box is isolated from the 2DEG region, leading to a decrease in the width of the Lorentzian-shaped resonance.

B. Rectangular antidot lattice

The motion of conduction electrons under the influence of a 2D periodic antidot potential has attracted considerable interest.[5,21–23] Small circular high-resistive regions are surrounded by a high mobility 2DEG, so that electrons move ballistically between collisions with antidots. Transport properties can be modified by the artificial impurities. The array of scattering centers is generated by various technologies including gate electrode with dielectric material,[21] shallow etching,[22] and focused ion-beam implantation.[23] The effective diameter of the antidot is increased by the depletion length. Hence, it is not easy with the present technology to achieve a diameter of the antidot smaller than the Debye length. Commensurability of the cyclotron orbit diameter and the period of the antidot lattice,[22] which is one of the remarkable results revealed in the experiments, is basically based on a classical effect. However, the rapid advances in nanofabrication[24] and crystal growth[25] technologies will make it possible to realize the structure of the periodicity comparable with the Fermi wavelength. By use of a scanning tunneling microscope tip, it may become possible to put impurities in 2DEG so as to consist of a periodic impurity lattice.[26] As will be discussed, quantum-mechanical effects play an important role in the transport property in such structures.[27]

For the 2D array of antidots shown in Fig. 1(b), the periodic potential is given within the assumption of the δ-function potential modulation as

$$V(x,y)=U\sum_{i=0}^{N_x}\delta(x-ia)\sum_{j=0}^{N_y}\delta(y-ja)\ . \tag{29}$$

In the uniform waveguide sections we have $f_{nm}=\delta_{nm}$. The generalized boundary condition is given, instead of (14), by[13]

$$\left.\frac{dc_n(x)}{dx}\right|_{x=ia+\varepsilon}-\left.\frac{dc_n(x)}{dx}\right|_{x=ia-\varepsilon}=\frac{2mU}{\hbar^2}\sum_l V_{nl}c_l(ia)\ , \tag{30}$$

where

$$V_{nl}=\frac{2mU}{\hbar^2}\int u_n(y)\sum_j\delta(y-ja)u_l(y)dy \tag{31a}$$

$$=\begin{cases}\gamma N_y\ , & |n-l|2iN_y \text{ and } n+l\neq 2jN_y\\ -\gamma N_y\ , & |n-l|\neq 2iN_y \text{ and } n+l=2jN_y\\ 0 \text{ otherwise}\ ,\end{cases} \tag{31b}$$

with $\gamma=2mU/\hbar^2W$ and $i,j=0,1,2,\ldots$. In general, the two-dimensionally localized potential mixes all different

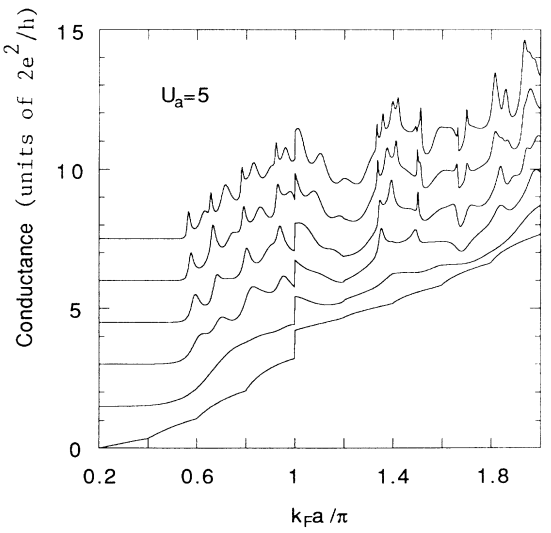

FIG. 6 Conductance (in units of $2e^2/h$) for repulsive antidot lattices with $N_y=5$. The curves, from top to bottom, correspond to $N_x=5$ to $N_x=0$, respectively. The quantized step at $k_Fa/\pi=1$, where half of the Fermi wavelength coincides with the periodicity, is unaffected by the antidots. The strength of the antidot potential considered is $U_a=5$. The curves are offset by $1.5\times 2e^2/h$ for clarity.

modes including the evanescent modes. Distributing scatterers regularly, however, the mode coupling is allowed only among specific modes. Instead of (17) one obtains the relation

$$C_n=\sum_m \left[\left[\delta_{mn}-i\frac{V_{nm}}{2k_n} \right] e^{ik_m a} A_m - i\frac{V_{nm}}{2k_n} B_m \right] , \quad (32a)$$

$$D_n=\sum_m \left[i\frac{V_{nm}}{2k_n} e^{i(k_m-k_n)a} A_m + \left[\delta_{mn}+i\frac{V_{nm}}{2k_n} \right] e^{-ik_m a} B_m \right] . \quad (32b)$$

Figure 6 shows the conductance of an array of antidots as a function of $k_F a/\pi$. Four δ-function potentials (repulsive impurities) are placed in the y direction while the number in the x direction is varied from one to six. The dimensionless amplitude of the antidot potential is $U_a \equiv mU/\hbar^2=5$. The location of the antidots is chosen so that the quantized steps at $k_F a/\pi=1$ are not affected by the antidots. One can see that the antidot potential alters the transmission coefficient significantly. The quantized plateau in a perfect wire is smeared by superimposing a single column of antidots. The remnant of the quantized plateau is almost smoothed out when $N_x=1$. Further increase of N_x results in multiple peaks due to constructive and destructive electron scattering from the antidots. It is interesting to note that nearly complete opaqueness is achieved for $N_x \geq 2$, even for an energy range where propagating modes already exist in the external leads. If a single impurity is placed randomly in the wire, a finite conductance is obtained throughout the entire range of energies.[13,28]

The scattered waves at large distances from the scattering center are described by

$$\psi_{sc}(\theta)=\sum_{i=1}^{M} f(\theta) e^{ik_F r_i}/r_i , \quad (33)$$

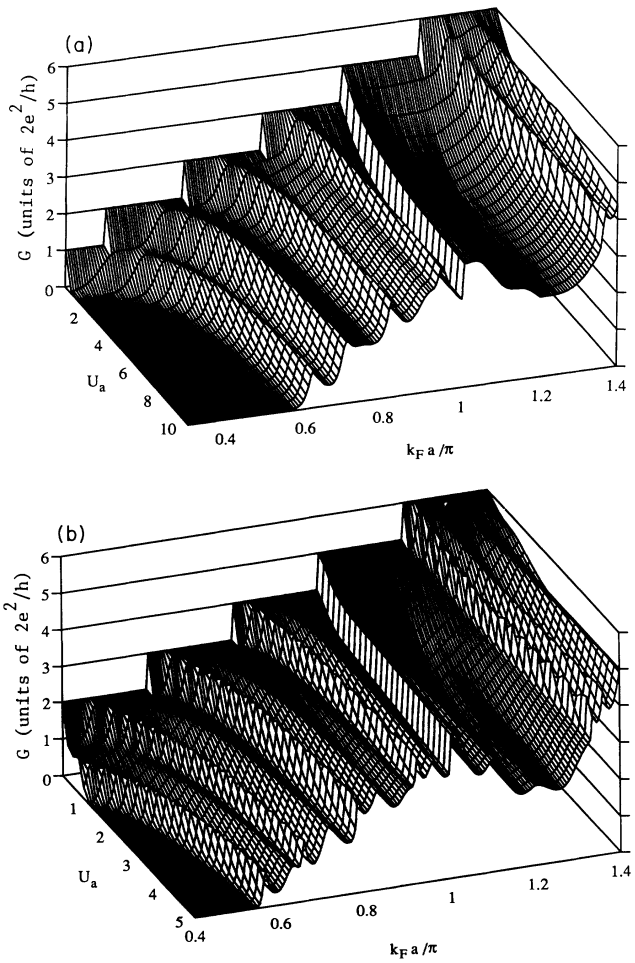

FIG. 7. Two-terminal conductance (in units of $2e^2/h$) is plotted as a function of the dimensionless strength of the antidot potential U_a and $k_F a/\pi$ for 2D lattices of repulsive antidots with (a) $N_x=3$, $N_y=5$, and (b) $N_x=N_y=5$. A "miniband" is formed around $k_F a/\pi=1$ as the antidot lattice is introduced in 2DEG.

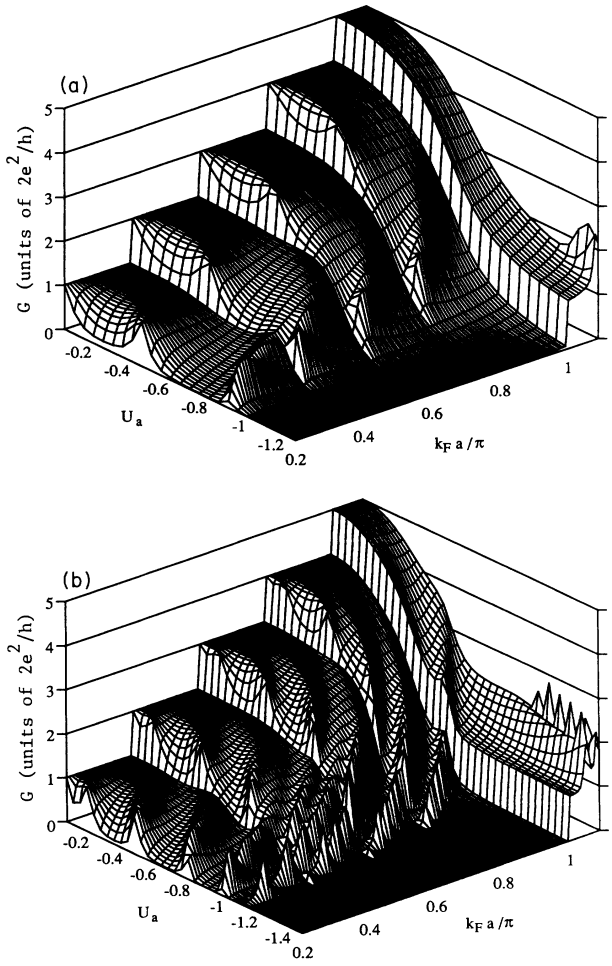

FIG. 8. Three-dimensional representations of the conductance (in units of $2e^2/h$) of attractive antidot lattices as functions of $k_F a/\pi$ and the strength of the potential U_a. The size of the lattices is (a) $N_x=2$ and $N_y=5$, and (b) $N_x=N_y=5$. As the scatterer is made more attractive, dips corresponding to the transmission resonances due to the quasibound states move lower in energy and disappear if they fall below the bottom of the subband.

where M is the number of impurities, $f(\theta)$ is the scattering amplitude caused by a single impurity, and r_i is the distance from the ith scattering center. The probability density in the θ direction is

$$|\psi_{sc}(\theta)|^2 = M^{\nu}|f(\theta)|^2/R^2 , \tag{34}$$

where R is the average distance from the scattering center. If the distribution of the impurities is random, the interference terms vanish because the phases of the wave functions differ significantly and will usually ensemble average (we do not consider weak localization here). As a result, we have $\nu=1$. On the other hand, for a regular impurity lattice, constructive interference between electrons and the scattering center can lead to $\nu=2$, if the relations

$$k_F(r_i - r_j) = 2m\pi \tag{35}$$

are satisfied.[27] Therefore, efficient control of the electron transmission by a small number of impurities and electron diffraction can be expected.[27,29]

The influence of the antidot potential is shown in Fig. 7 as a function of the strength of the antidot potential U_a and of $k_F a/\pi$. The threshold energy for overall transmission through the antidot lattice is increased with increasing U_a. Hence, a "miniband" is formed around $k_F a/\pi = 1$ and a broad dip, which is similar to the formation of a minigap though complete reflection is not achieved, appears near $k_F a/\pi = 1.2$. In experiments on a 2D array of large antidots (network of quasi-one-dimensional wires), structure in the conductance has been observed by Smith *et al.* and was associated with Bragg reflection.[8]

In Fig. 8, we show the two-terminal conductance for a lattice of attractive scatterers. In contrast to the repulsive potential, the attractive potential induces quasibound states which split off from one of the evanescent modes. A drastic change is induced even by weak potential. As the potential is made more attractive, the overall conductance decreases and new dips corresponding to the quasibound states move lower in energy.[13,28] The dips disappear when the potential is sufficiently attractive that they are lowered below the bottom of the subbands. The number of peaks as U_a is varied is equal to N_x. Figure 9 shows several slices for fixed U_a. When the strength of the scatterer is further increased, the conductance resembles that through the repulsive antidot lattice.[13] A broad dip of nearly perfect reflection, which is classically unexpected for an attractive potential, is seen below $k_F a/\pi \sim 1$ even when the potential is relatively weak. The threshold of overall propagation and peaks due to quantum interference move lower in energy when the scatterer is made more attractive, indicating that this behavior arises from the transmission resonances through the quasibound states.

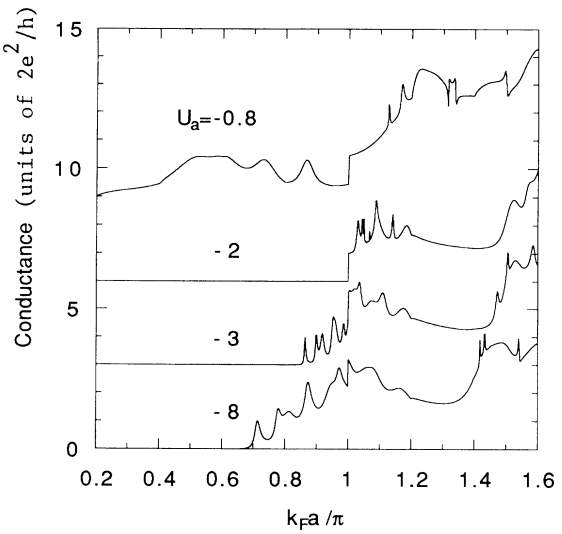

FIG. 9. Conductance (in units of $2e^2/h$) for 2D attractive antidot lattices with $N_x=3$ and $N_y=5$. The dimensionless strength of the antidot potential is $U_a=-0.8$, -2, -3, and -8 from top to bottom. The transmission thresholds move lower in energy as the potential is made more attractive. The curves are offset by $3\times 2e^2/h$ for clarity.

IV. SUMMARY

A numerical analysis of finite-size 1D and 2D lateral superlattices and various rectangular arrays of antidots has been presented. Transmission and reflection properties of an electron are evaluated by utilizing a mode-matching method for electron waveguides. We use these transmission probabilities to obtain the two-terminal conductance through a periodic potential modulation. In the energy dependence of the conductance, a formation of minibands, which are composed of almost dispersionless states, in finite superlattices gives rise to strong oscillation regions which are separated by broad dips of zero conductance due to minigaps. It is found that the lower edge of the minibands is increased when the superlattice potential is made strong, whereas the higher edge is independent of the strength and the size of the superlattice (a result expected from simple Kronig-Penney models). When short-range scatterers are placed in the 2DEG so as to consist of a periodic lattice, the transport properties are modified because of coherent interaction between electrons and scatterers. By increasing the number of columns of impurities, the conductance is made to reveal an oscillation which resembles a Bloch band structure appearing as a broad dip. Quasibound states, provided by an attractive antidot lattice, give rise to a total reflection over a wide range of energy and strength of the potential.

ACKNOWLEDGMENTS

The authors are grateful to K. Yano and Q. Li for helpful discussions. This work was supported in part by the Office of Naval Research.

[1]H. Sakaki, K. Wagatsuma, J. Hamasaki, and S. Saito, Thin Solid Films **36**, 497 (1976).

[2]D. K. Ferry, Phys. Status Solidi B **106**, 63 (1981); R. K. Reich, R. O. Grondin, D. K. Ferry, and G. J. Iafrate, Phys. Lett. **91A**, 28 (1982); R. K. Reich, R. O. Grondin, and D. K. Ferry, Phys. Rev. B **27**, 3483 (1983); R. O. Grondin, W. Porod, J. Ho, D. K. Ferry, and G. J. Iafrate, Superlatt. Microstruct. **1**, 183 (1985); K. Tsubaki and Y. Tokura, Appl. Phys. Lett. **53**, 859 (1988); K. Ismail, W. Chu, D. A. Antoniadis, and H. I. Smith, *ibid.* **52**, 1071 (1988).

[3]R. R. Gerhardts, D. Weiss, and K. von Klitzing, Phys. Rev. Lett. **62**, 1173 (1989); R. W. Winkler, J. P. Kotthaus, and K. Ploog, *ibid.* **62**, 1177 (1989).

[4]G. Bernstein and D. K. Ferry, J. Vac. Sci. Technol. B **5**, 964 (1987); E. Paris, J. Ma, A. M. Kriman, D. K. Ferry, and E. Barbier, J. Phys. Condens. Matter **3**, 6605 (1991); J. Ma, R. Puechner, W. P. Liu, A. M. Kriman, G. N. Maracs, and D. K. Ferry, Surf. Sci. **229**, 341 (1990).

[5]R. R. Gerhardts, D. Weiss, and U. Wulf, Phys. Rev. B **43**, 5192 (1991).

[6]L. Esaki and R. Tsu, IBM J. Res. Develop. **14**, 61 (1970).

[7]*Granular Nanoelectronics,* edited by D. K. Ferry, J. R. Barker, and C. Jacoboni (Plenum, New York, 1991).

[8]C. G. Smith, M. Pepper, R. Newbury, H. Ahmed, D. G. Hasko, D. C. Peacock, J. E. F. Frost, D. A. Ritchie, G. A. C. Jones, and G. Hill, J. Phys. Condens. Matter **2**, 3405 (1990).

[9]R. Dingle, A. C. Gossard, and W. Wiegmann, Phys. Rev. Lett. **34**, 1327 (1975).

[10]S. E. Ulloa, E. Castano, and G. Kirczenow, Phys. Rev. B **41**, 12 350 (1990).

[11]L. P. Kouwenhoven, F. W. J. Hekking, B. J. van Wees, C. J. P. M. Harmans, C. E. Timmering, and C. T. Foxon, Phys. Rev. Lett. **65**, 361 (1990).

[12]R. L. Schult, H. W. Wyld, and D. G. Ravenhall, Phys. Rev. B **41**, 12 760 (1990); G. Kirczenow, Phys. Rev. Lett. **62**, 2993 (1989); Y. Avishai and Y. P. Band, *ibid.* **62**, 2527 (1989).

[13]P. F. Bagwell, Phys. Rev. B **41**, 10 354 (1990).

[14]H. Kasai, K. Mitsutake, and A. Okiji, J. Phys. Soc. Jpn. **60**, 1679 (1991).

[15]R. Landauer, Philos. Mag. **21**, 863 (1970); R. Landauer, J. Phys. Condens. Matter **1**, 8099 (1989); D. S. Fisher and P. A. Lee, Phys. Rev. B **23**, 6851 (1981); M. Büttiker, Y. Imry, R. Landauer, and S. Pinhas, *ibid.* **31**, 6207 (1985).

[16]G. Kirczenow, J. Phys. Condens. Matter **1**, 305 (1989).

[17]C. G. Smith, M. Pepper, H. Ahmed, J. E. F. Frost, D. G. Hasko, D. C. Peacock, D. A. Ritchie, and G. A. C. Jones, J. Phys. C **21**, L893 (1988).

[18]Y. Hirayama and T. Saku, Solid State Commun. **73**, 113 (1990).

[19]M. Y. Azbel, Phys. Rev. B **28**, 4106 (1983).

[20]Y. Imry, in *Directions in Condensed Matter Physics,* edited by G. Grinstein and G. Mazenko (World Scientific, Singapore, 1986); D. A. Wharam, T. J. Thornton, R. Newbury, M. Pepper, H. Ahmed, J. E. F. Frost, D. G. Hasko, D. C. Peacock, D. A. Ritchie, and G. A. C. Jones, J. Phys. C **21**, L209 (1988); B. J. van Wees, H. van Houten, C. W. J. Beenakker, J. G. Williamson, L. P. Kouwenhoven, D. van der Marel, and C. T. Foxon, Phys. Rev. Lett. **60**, 848 (1988).

[21]E. S. Alves, P. H. Beton, M. Henini, L. Eaves, P. C. Main, O. H. Hughes, G. A. Toombs, S. P. Beaumont, and D. W. Wilkinson, J. Phys. Condens. Matter **1**, 8257 (1989).

[22]D. Weiss, M. L. Roukes, A. Menschig, P. Grambow, K. von Klitzing, and G. Weimann, Phys. Rev. Lett. **66**, 2790 (1991); T. Yamashiro, J. Takahara, Y. Takagaki, K. Gamo, S. Namba, S. Takaoka, and K. Murase, Solid State Commun. **79**, 885 (1991).

[23]K. Ensslin and P. M. Petroff, Phys. Rev. B **41**, 12 307 (1990); J. Takahara, T. Kakuta, T. Yamashiro, Y. Takagaki, T. Shiokawa, S. Takaoka, K. Gamo, K. Murase, and S. Namba, Jpn. J. Appl. Phys. **30**, 3250 (1991).

[24]B. P. van der Gaag and A. Scherer, Appl. Phys. Lett. **56**, 481 (1990).

[25]T. Fukui, S. Ando, Y. Tokura, and T. Toriyama, Appl. Phys. Lett. **58**, 2018 (1991).

[26]D. M. Eigler and E. K. Schweizer, Nature **344**, 524 (1990).

[27]K. Furuya, Jpn. J. Appl. Phys. **30**, L82 (1991).

[28]K. Takagaki and D. K. Ferry, Phys. Rev. B **45**, 6715 (1992).

[29]K. Furuya, J. Appl. Phys. **62**, 1492 (1987).

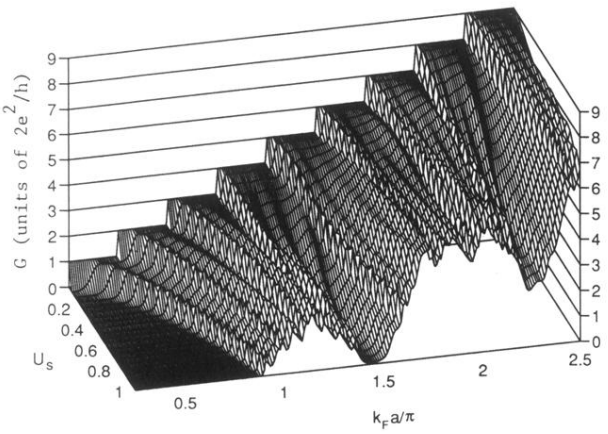

FIG. 5. Conductance (in units of $2e^2/h$) for a two-dimensional lateral surface superlattice with $N_x = N_y = 4$ as functions of U_s and $k_F a/\pi$. When the superlattice potential is introduced, N_y subbands merge into a miniband and minigaps open between the minibands. The lower edge of the minibands becomes higher in energy as U_s is increased.

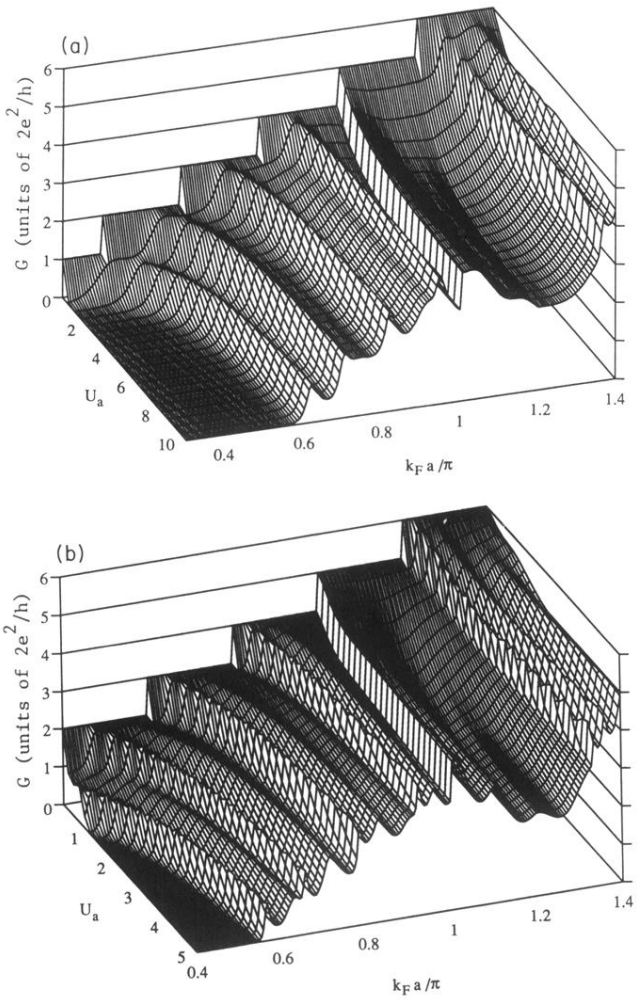

FIG. 7. Two-terminal conductance (in units of $2e^2/h$) is plotted as a function of the dimensionless strength of the antidot potential U_a and $k_F a/\pi$ for 2D lattices of repulsive antidots with (a) $N_x=3$, $N_y=5$, and (b) $N_x=N_y=5$. A "miniband" is formed around $k_F a/\pi=1$ as the antidot lattice is introduced in 2DEG.

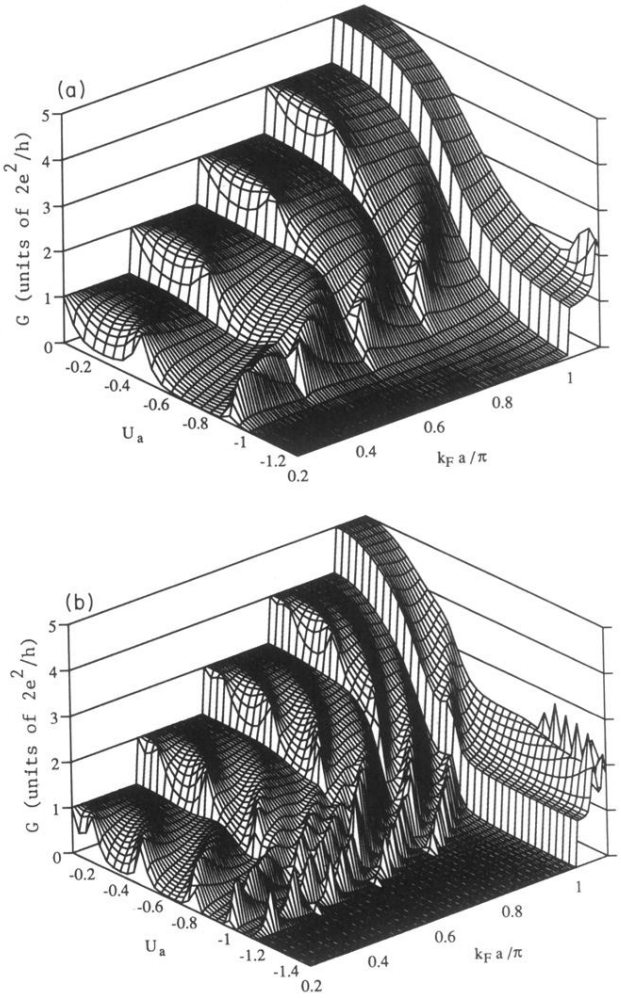

FIG. 8. Three-dimensional representations of the conductance (in units of $2e^2/h$) of attractive antidot lattices as functions of $k_F a/\pi$ and the strength of the potential U_a. The size of the lattices is (a) $N_x=2$ and $N_y=5$, and (b) $N_x=N_y=5$. As the scatterer is made more attractive, dips corresponding to the transmission resonances due to the quasibound states move lower in energy and disappear if they fall below the bottom of the subband.